LIFE SCIENCES

Hierarchical assembly governs TRIM5α recognition of HIV-1 and retroviral capsids

Katarzyna A. Skorupka[1], Marcin D. Roganowicz[1], Devin E. Christensen[2], Yueping Wan[1], Owen Pornillos[1]*, Barbie K. Ganser-Pornillos[1]*

Copyright © 2019 The Authors, some rights reserved; exclusive licensee American Association for the Advancement of Science. No claim to original U.S. Government Works. Distributed under a Creative Commons Attribution NonCommercial License 4.0 (CC BY-NC).

TRIM5α is a restriction factor that senses incoming retrovirus cores through an unprecedented mechanism of nonself recognition. TRIM5α assembles a hexagonal lattice that avidly binds the capsid shell, which surrounds and protects the virus core. The extent to which the TRIM lattice can cover the capsid and how TRIM5α directly contacts the capsid surface have not been established. Here, we apply cryo–electron tomography and subtomogram averaging to determine structures of TRIM5α bound to recombinant HIV-1 capsid assemblies. Our data support a mechanism of hierarchical assembly, in which a limited number of basal interaction modes are successively organized in increasingly higher-order structures that culminate in a TRIM5α cage surrounding a retroviral capsid. We further propose that cage formation explains the mechanism of restriction and provides the structural context that links capsid recognition to ubiquitin-dependent processes that disable the retrovirus.

INTRODUCTION

Mammalian cells express a variety of innate immune receptors that sense the presence of invading viruses and induce defensive countermeasures. TRIM5α is an E3 ubiquitin ligase that senses incoming retroviruses by binding to the capsid coat that protects the viral core, subsequently inducing premature core dissociation and inhibiting reverse transcription of the viral genome [(*1*, *2*) and reviewed in (*3*)]. TRIM5α recognizes retroviral capsids by assembling a lattice with complementary hexagonal symmetry and spacing to the capsid lattice, thereby aligning otherwise very weak interaction epitopes and enabling avid binding (*4*). Structural insights on the TRIM5α lattice have been derived from crystallographic studies of oligomeric subcomplexes and low-resolution cryo–electron microscopy of biochemically reconstituted TRIM5α/capsid complexes (*4*–*8*). However, the extent to which the TRIM lattice can cover the capsid and how TRIM5α directly contacts the capsid surface have not been established.

Retroviral capsids are organized as fullerene structures comprising several hundred viral CA protein hexamers and 12 CA pentamers (*9*, *10*). These capsids display a remarkable degree of polymorphism [reviewed in (*11*)]. For example, a typical HIV-1 capsid is cone shaped and displays highly variable surface curvature (*9*, *10*). These capsids can also be cylindrical, spherical, or polyhedral; the different shapes arise from differing distributions of the hexamers and pentamers (*12*). Individual capsids can use different numbers of CA subunits (ranging from around 1200 to around 2000), and so capsid size can also vary. Thus, there is considerable structural variation both within a single capsid particle and across different capsids, even within a single retrovirus species. To function effectively, TRIM5α must have requisite flexibility to accommodate these variations, yet the molecular basis of such flexibility is not yet fully established.

Purified recombinant HIV-1 CA proteins can assemble in vitro into long helical tubes that recapitulate the structural and functional properties of the hexagonal capsid lattice (*13*, *14*). TRIM5α-bound HIV-1 CA tubes can also be reconstituted in vitro (*7*, *8*). We applied cryo–electron tomography and subtomogram averaging on these complexes to obtain a series of reconstructions that collectively describe how the TRIM5α lattice recognizes and binds the HIV-1 capsid lattice. Our maps show that the TRIM5α capsid-binding domains act as dimeric units and contact the capsid surface in multiple different ways. These contacts are organized in a hierarchy of structures, which constitute a TRIM5α lattice that completely cages a retroviral capsid.

RESULTS

We reconstituted TRIM5α/capsid complexes by coincubating purified TRIM5α and HIV-1 CA proteins (*7*, *8*). Cryotomograms of the resulting tubes, collected at high defocus values (high contrast), exhibited patches of clearly resolved, large hexagonal rings on the tube surface (Fig. 1A). Thus, binding of TRIM5α to the capsid-like tubes was evident in individual raw images. To visualize higher resolution, we performed subtomogram averaging (*15*) of seven tubes from low-defocus cryotomograms. Each CA tube belongs to a distinct helical family with differing diameter (fig. S1). Collectively, the tubes therefore sample the structural variations found within authentic capsids (but not pentamer-containing declinations).

Average structures were calculated for the CA hexamer (the repeating unit of the capsid-like tubes) (fig. S2, A and B) and the TRIM5α trimer and dimer (the repeating units of the TRIM lattice) (fig. S3, A and B). For cross-validation, we independently calculated the trimer and dimer averages (Fig. 1, C and D, and fig. S3A), which confirmed that their refined positions and orientations defined the same lattice in each tube (Fig. 1E). Both the two- and threefold positions were resolved in each of the dimer and trimer maps, and their overlapping regions show excellent agreement (fig. S3, B to D). The nominal resolutions of the individual reconstructions are 17 Å (hexamer), 26 Å (dimer), and 25 Å (trimer) (figs. S2C and S3E).

We visualized the global architecture of the TRIM5α/capsid complexes by generating lattice maps from the positions and orientations of subunit densities as determined by subtomogram averaging (Fig. 1, B to E). The tubes consist of an inner wall of CA hexamers, similar to previous helical reconstructions (Fig. 1B) (*13*, *14*). The

[1]Department of Molecular Physiology and Biological Physics, University of Virginia, Charlottesville, VA, USA. [2]Department of Biochemistry, University of Utah, Salt Lake City, UT, USA.
*Corresponding author. Email: bpornillos@virginia.edu (B.K.G.-P.); opornillos@virginia.edu (O.P.)

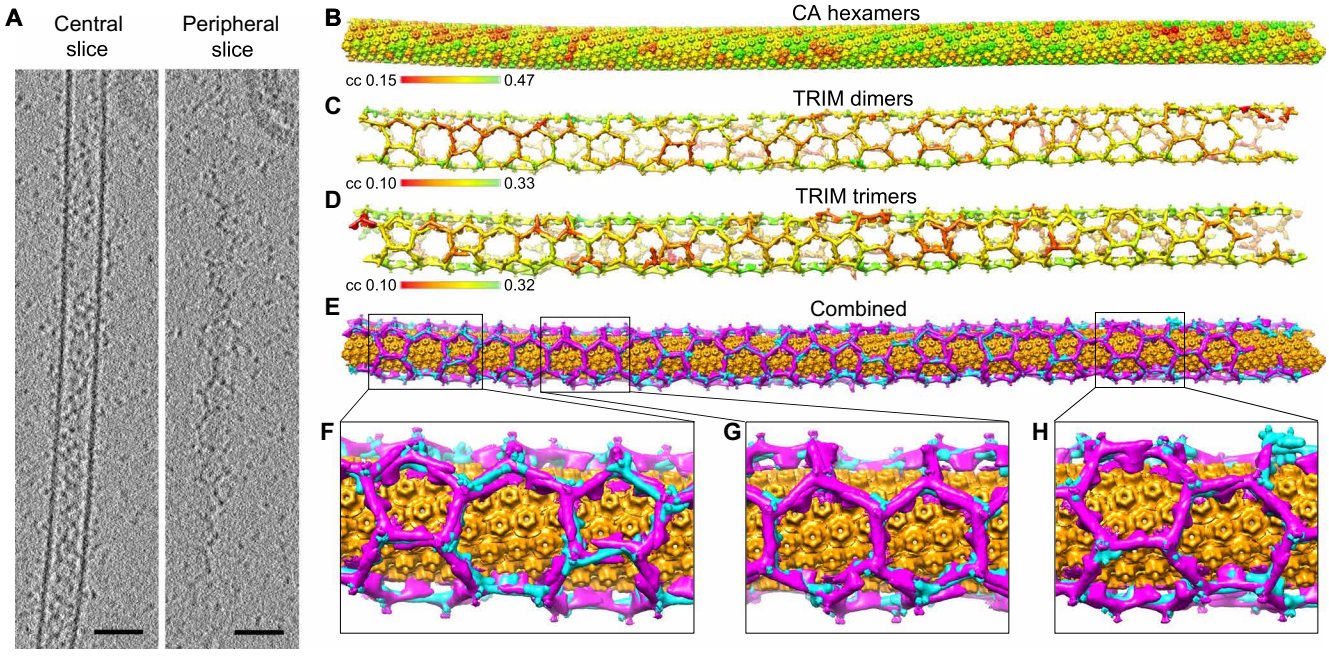

Fig. 1. Cryotomography and subtomogram averaging of TRIM5α-coated HIV-1 capsid-like tubes. (**A**) Sections from a tomogram collected at high defocus values (~9 μm), emphasizing the walls of the CA tube (central slice) and the surrounding TRIM5α lattice (peripheral slice). Scale bars, 100 nm. (**B** to **D**) Lattice maps showing the final positions and orientations of CA hexamers (B), TRIM dimers (C), and TRIM trimers (D) from a single tube. Each position is displayed on a color scale of red to green, from low to high cross-correlation value as indicated. (**E**) Combined lattice map with CA hexamers colored in orange, TRIM dimers in cyan, and TRIM trimers in magenta. (**F** to **H**) Close-up views.

TRIM5α proteins make an essentially contiguous network of interactions, forming a hexagonal wire cage that completely surrounds the CA tube (Fig. 1, C to E).

Like other tripartite motif family members, TRIM5α contains an N-terminal RBCC motif—consisting of RING, B-box 2, and coiled-coil domains—followed by a SPRY domain that directly binds the capsid (Fig. 2A). The coiled-coil domain forms a long α helix that dimerizes in an antiparallel orientation, making an elongated rod that is capped at each end by the B-box 2 domain (*5*, *6*). The B-box 2 domain makes a trimer that links dimers into a hexagonal lattice (*8*, *16*). Although our reconstructed maps are of limited resolution, fitting the crystal structures of B-box 2/coiled-coil dimers (*6*) and trimers (*8*) resulted in an unambiguous solution (Fig. 2, B to E, and fig. S4). This is because both the B-box 2/coiled-coil trimer crystal structure (*8*) and our corresponding trimer reconstruction here have pronounced curvature, with the concave surface facing the capsid. In the fitted model, the N-terminal end of the B-box 2 domain is found on the cytoplasmic (convex) face of the trimer, whereas the C-terminal end of the coiled-coil domain is found on the capsid (concave) side. Our interpretation is further bolstered by an additional density feature on the cytoplasmic side of the B-box 2 trimer and adjacent to the fitted B-box N termini. This extra density becomes more pronounced at low contour levels (fig. S5A), and we established that it is due to the RING domain by comparison with reconstructions from TRIM5α/CA complexes made with a TRIM5α RING deletion mutant (fig. S5B). Our reconstructions therefore confirm the proposed organization of the TRIM5α hexagonal lattice that was deduced from isolated structures of the subcomplexes (*8*).

After modeling the RBCC domains, the only remaining density feature projects downward from the center of the coiled coil, which

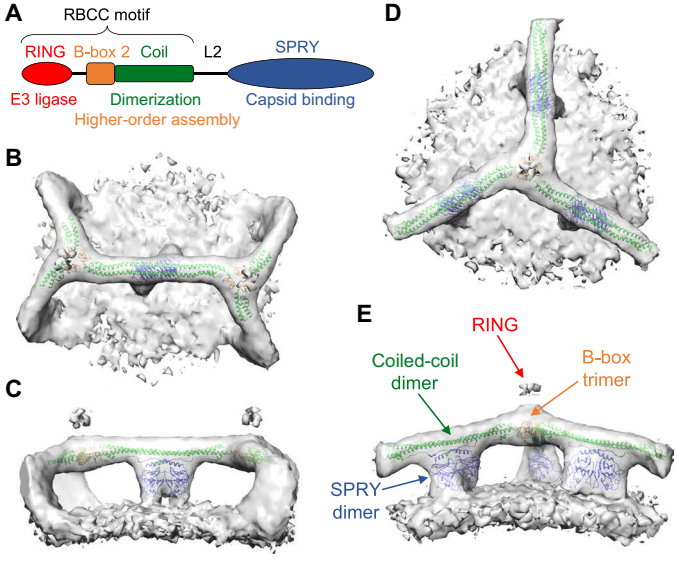

Fig. 2. The structure of TRIM5α bound to HIV-1 capsid-like tubes. (**A**) Domain organization of TRIM5α. (**B** to **E**) Orthogonal views of subtomogram-averaged structures centered on the TRIM5α dimer (B and C) and trimer (D and E). Each map is shown as an isosurface, with a composite PDB model obtained by rigid-body docking of crystal structures (as described in the main text; see also fig. S5). The domains are colored as in (A): B-box 2, orange; coiled coil, green; and SPRY, blue.

we therefore assigned to the SPRY domain (Fig. 2, C and E). This assignment is consistent with previous analyses, including difference density comparisons of flattened TRIM5α lattices, which also localized SPRY to the center of the hexagon edges (*4*, *7*). The SPRY

density appears as a symmetric closed-packed dimer, even in the trimer reconstruction, which was averaged with imposed threefold (but not twofold) symmetry (fig. S3B). This observation supports the proposal that the two SPRY domains within a TRIM5α dimer act as a single bivalent unit that simultaneously engages two binding epitopes (*5*, *6*, *8*, *17*). In the dimer reconstruction, the SPRY density is more clearly bilobed and flares out before joining with the capsid surface (Fig. 3, A and B). Guided by overlapping residues in separate crystal structures of the coiled-coil and SPRY domains (*6*, *18*, *19*), a computational model of the coiled-coil/SPRY substructure was generated (*17*). Fitting of this model positions two copies of SPRY well within the dimeric density, with only minimal adjustments (fig. S4). Although more precise details will have to await an experimentally determined higher-resolution structure, our SPRY domain positioning satisfies multiple constraints from previous studies. Each SPRY domain is packed against the coiled coil through a short helix and an amphipathic interface previously shown to be important for capsid binding and restriction (*17*, *20*). The V1 loops are positioned at the flared regions that contact the capsid surface (magenta in Fig. 3, A and B), consistent with studies indicating that V1 directly binds the CA subunits (*18*, *19*, *21*–*23*). Furthermore, our model also suggests that a short segment ($_{430}$IVPLSVIIC$_{438}$ in rhesus TRIM5α) that includes the outermost strand of the SPRY β-sandwich fold may mediate lateral SPRY/SPRY contacts (asterisk in Fig. 3A). The V435K/I436K mutations within this segment were previously shown to disrupt capsid binding and restriction activity (*24*).

In the averaged CA reconstruction, the hexamers are well defined (Fig. 1B), whereas in both the TRIM dimer and trimer maps, the capsid surface is essentially featureless (Fig. 2, B to E). This indicates that the SPRY domains adopt multiple different orientations relative to the underlying CA hexamers. To examine this further, we projected the centroid SPRY dimer positions onto the same plane and analyzed their distribution relative to the nearest seven CA hexamers (with the hexamer closest to the SPRY in the center) (Fig. 3, C and D). Although the distribution showed substantial overall scatter, clustering was also evident, which appeared most pronounced above the three capsid symmetry axes (Fig. 3C). These results not only show that the SPRY dimer indeed has a degenerate set of binding modes relative to the CA hexamer but also suggest that certain binding modes are preferred. The clustering pattern has pronounced anisotropy that follows the long axis of the capsid tube. This provides further support for the notion that the assembling TRIM lattice can detect the curvature of the underlying CA lattice.

Guided by the lattice maps, we identified and extracted 550 subvolumes that each encompassed an entire TRIM hexagon. After an initial round of refinement, the resulting map had well-defined densities for the TRIM5α hexagon, and one of the helical lines for the capsid lattice was resolved (fig. S6A). This indicated to us that the average was composed of only a discrete number of configurations. The subvolumes could be classified into two subsets: Class 1 having 335 particles and Class 2 having 215 particles. The two classes differ in the relative rotation of the TRIM hexagon relative to the long axis of the CA tube (fig. S6B). In the Class 2 average, two helical lines of the capsid lattice were now visible, whereas in the Class 1 average, the CA hexamers were resolved. We therefore focused on Class 1. Two additional refinement rounds produced a map in which both the TRIM hexagon and underlying CA hexamers are resolved and interpretable (Fig. 4A and fig. S6D). In this reconstruction, the TRIM hexagon covers an area equivalent to about 11 CA hexamers. All six SPRY domain dimers in the hexagon edges and connecting densities to the CA hexamers are visible. We observed four distinct modes of SPRY/CA interactions (Fig. 4B). SPRY dimers connect two adjacent CA hexamers in edges ii, iv, and v, with edge ii having the opposite handedness as edges iv and v. In edges iii and

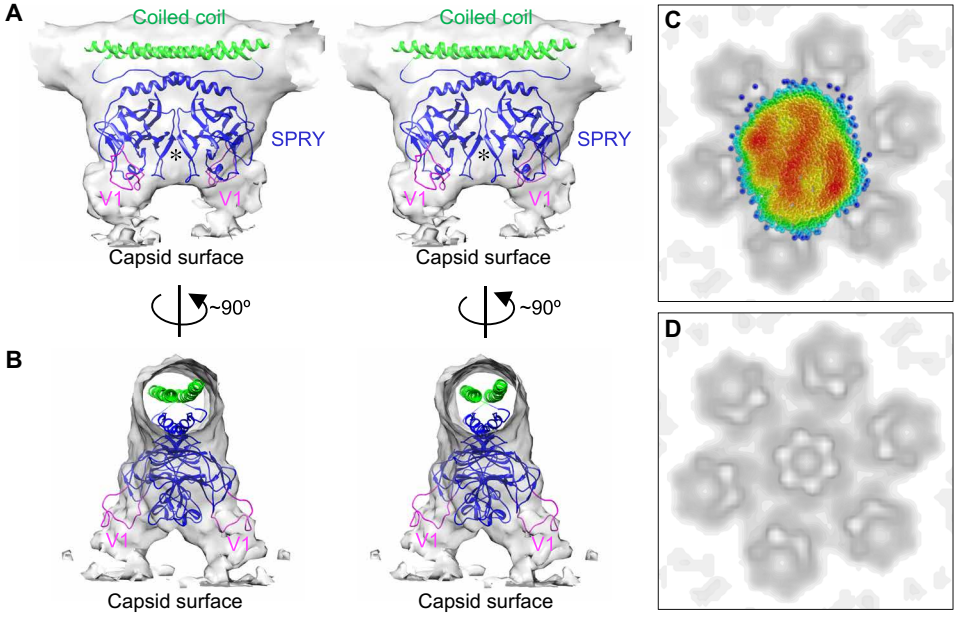

Fig. 3. The SPRY domain binds to the capsid surface. (**A** and **B**) Orthogonal stereoviews of the SPRY dimer reconstruction, with modeled coiled-coil/SPRY dimer. The flexible V1 loops (magenta), which are predicted to directly contact CA are located at the flared regions that join with the capsid surface. A putative SPRY/SPRY dimer interface is indicated by an asterisk. (**C**) Scatter plot of SPRY dimer positions relative to the closest CA hexamers. Points are colored according to a color gradient that indicates the degree of clustering (red, highest point density and blue, lowest point density). (**D**) Projection of the CA hexamers in (C), shown for reference.

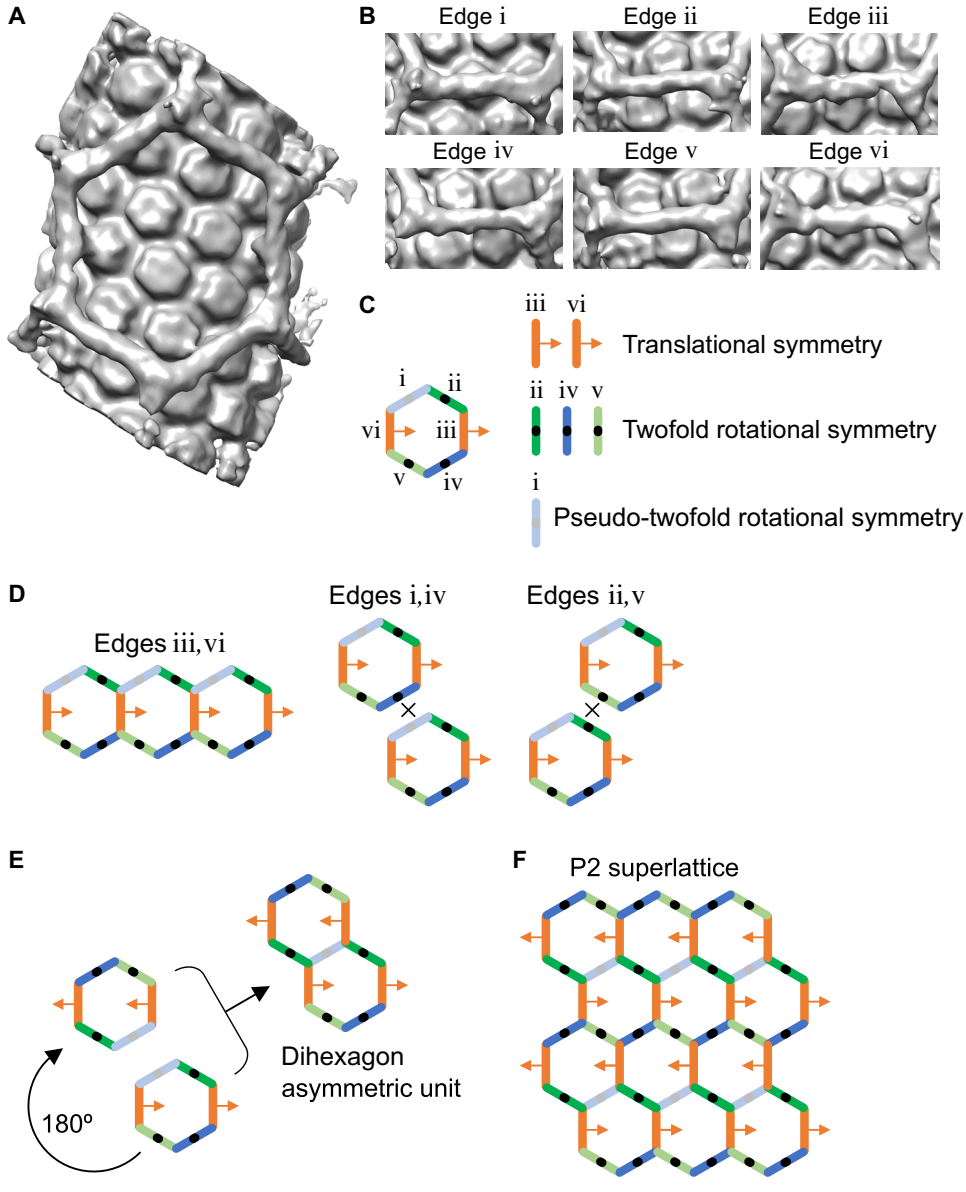

Fig. 4. Structure of TRIM5α in complex with the HIV-1 capsid lattice. (**A**) Average reconstruction. (**B**) Views of each of the six edges in the same orientation. (**C**) Schematic representation of the structure as a hexagon with structurally distinct edges in different colors and labeled from i to vi as shown. Legend indicates the symmetry properties of each edge, which describe the relative arrangements of SPRY and CA. (**D**) Tiling of a single hexagon is possible only along the iii,vi edge pair trajectory but not the i,iv or ii,v trajectories. (**E**) Construction of a dihexagon asymmetric unit from the hexagon unit. (**F**) Tessellation of the dihexagon into a planar lattice.

vi, the SPRY dimer is positioned asymmetrically above a single CA hexamer. Last, in edge i, the SPRY dimer is almost directly above a CA hexamer. We therefore conclude that indeed, TRIM5α contacts the capsid surface in a degenerate manner, but the SPRY domains have preferred modes of binding to the CA subunits. Although a more accurate accounting of the actual number of SPRY/CA interaction modes and the precise details of how the SPRY V1 loops contact the CA subunits will have to await further studies, such degenerate positioning agrees very well with results from mapping studies of susceptibility and resistance determinants on CA (*25–33*).

The Class 1 map is globally asymmetric because the two lattices are offset translationally. This is also evident from the nonsymmetric arrangement of the six hexagon edges (Fig. 4C). Therefore, the Class 1 map cannot be the repeating unit of a TRIM5α/CA superlattice (Fig. 4D). We therefore asked whether the Class 1 map represents a smaller portion of a larger asymmetric unit that can be tessellated (or tiled) into a superlattice. Because the TRIM hexagons must share edges, such a unit would require SPRY/CA contacts on opposite edges to be oriented in the same way or related by translational symmetry. This is only true for the iii,vi edge pair (Fig. 4D). However, three of the edges are formally twofold rotationally symmetric (edges ii, iv, and v), and one is pseudo-twofold symmetric (edge i) (Fig. 4, B and C). Therefore, one can generate a larger asymmetric unit—a dihexagon—of a putative TRIM5α/CA superlattice by rotating a

second copy of the map around edge i and then overlapping this with the equivalent edge in the first copy (Fig. 4E). This dihexagon can now be tessellated into a planar P2 lattice (Fig. 4F).

The above analysis explains how the TRIM hexagonal lattice can undergo limited extensions beyond the initial seed by using only four distinct types of SPRY/CA contacts. But how can TRIM5α cover the entire capsid lattice? Closer examination of the Class 2 particles indicated that these can be further classified into two additional subsets, which now differ from each other by translation relative to the underlying capsid lattice (fig. S6C). Unfortunately, the reconstructions cannot be improved further because of the limited number of particles. However, it is likely that, as with the Class 1 hexagon, these Class 2 hexagon subsets are also one-half of two other dihexagon units (or each is half of a single dihexagon unit). Regardless, we surmise that the Class 2 reconstructions present distinct arrangements of the same four types of SPRY/CA contacts identified in the Class 1 reconstruction.

Lattice mapping of the Class 1 and 2 particles revealed that these form separate patches of TRIM5α/CA superlattices in the tubes (Figs. 1, G and H, and 5). The patches are small, and each comprises only a few dihexagon units (Fig. 5, A and B). Because each patch differs in the relative rotation and translation of the TRIM lattice relative to the CA lattice, adjacent patches cannot be joined without creating a seam in one of the two lattices. The capsid lattice is contiguous in the tubes, and so it is the TRIM lattice that makes the adjustments by joining the TRIM hexagon patches with TRIM pentagons and heptagons (Figs. 1F and 5). Such a phenomenon—having small discrete patches of hexagonal lattice joined together by pentagon and heptagon insertions—is well documented in single-layer paracrystalline arrays of carbon graphene; the pentagon/heptagon insertions are called grain boundaries (*34*, *35*). We therefore conclude that just like graphene, the TRIM5 lattices assembled on the surfaces of the HIV-1 capsid tubes are paracrystalline, composed of small patches of hexagonal order joined together by pentagon- and heptagon-containing grain boundaries.

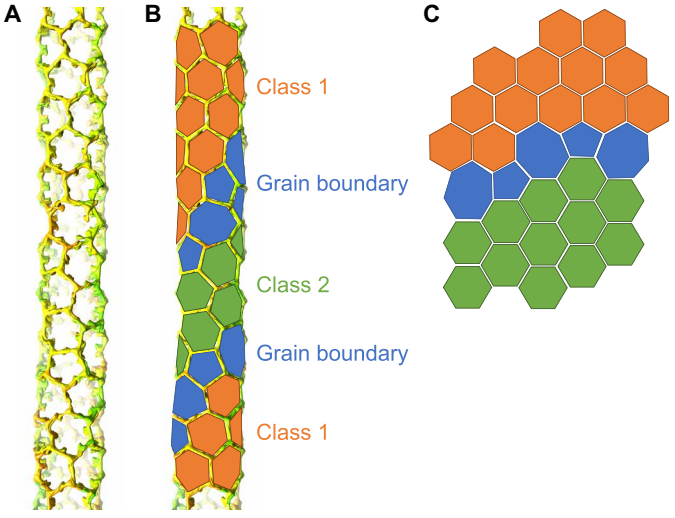

Fig. 5. Paracrystalline architecture of the TRIM5α lattice. (**A**) Lattice map of a TRIM5α-coated tube. CA hexamers are not shown for simplicity. (**B**) Same lattice map with geometric shapes traced and colored to aid in visualization. Class 1 hexagons are colored in orange, Class 2 hexagons in green, and grain boundary pentagons and heptagons in blue. (**C**) Illustration of two planar hexagonal lattice patches (orange and green) connected by pentagons and heptagons.

DISCUSSION

Although the lattice-lattice matching mechanism of capsid recognition by TRIM5α is now a well-established model (*3*), the molecular details have been quite challenging to characterize structurally. We and others have previously used a "divide-and-conquer" approach to obtain high-resolution x-ray crystal structures of the separate repeating structural units in the HIV-1 capsid and TRIM5 lattices (*6*, *8*, *16*, *36*). Our key goal in this current study is to deconstruct how conformational variations within the viral capsids are accommodated by the bound TRIM5 lattice, by using in vitro–assembled TRIM5α/HIV-1 CA complexes as a model system. Our studies also highlight the general challenge that is inherent to structural characterization of these types of systems, which arises from the fact that high-resolution structures are obtained by averaging structurally identical (or at least highly similar) particles. In this case, each tube that we examined (23 total, with 7 selected for analysis here) belongs to a different helical family and hence has a different diameter and degree of surface curvature. By using lattice mapping and subtomogram averaging (*15*), different structural subclasses that provide complementary structural information could be identified. Although gathering sufficient numbers of particles for high-resolution reconstruction of each subclass is significantly limiting, we nevertheless were able to generate a series of maps of sufficient resolution for meaningful interpretation, including a low-resolution map of part of an "asymmetric unit" of a putative TRIM5α/CA superlattice. By integrating the low-resolution reconstructions with previously determined x-ray crystal structures, we achieved a more sophisticated understanding of how TRIM5 proteins recognize and bind retroviral capsids.

The reconstructed maps of the TRIM5α dimer and trimer confirm the molecular architecture of the TRIM hexagonal lattice that we previously deduced from crystallographic structures of TRIM5 domain fragments (*8*). Our maps also provide direct experimental evidence that the two SPRY domains of a TRIM5α dimer are indeed bound to the center of the coiled-coil domain and form a close-packed dimeric unit as proposed (*5*, *6*, *8*, *17*), consistent with coordinated, simultaneous binding of the two SPRYs to CA.

By definition, a key feature of avidity-driven binding is the correspondence in relative spacing of the interacting elements (*37*), in this case between the TRIM5α SPRY domains and as yet unknown epitopes on the CA subunits. Ideally, these spacings are strictly matched, yet it is evident that this is unlikely with retroviral capsids, because their continuously varying curvature necessarily generates varying distances between equivalent surface epitopes on CA. Furthermore, TRIM5α must accommodate not only the variations in spacings but also variations in relative rotations of these equivalent epitopes, the retroviral capsids being made of CA hexamers and pentamers. Our studies now reveal that TRIM5α accomplishes this through hierarchical assembly, in which a limited number of basal interaction modes between the SPRY and CA subunits are successively organized in increasingly higher-order structures that culminate in a cage surrounding the retroviral capsid. Specifically, we identified at least four distinct types of basal SPRY/CA interactions that allow the SPRY domain to juxtapose the HIV-1 CA hexamer in multiple different ways. At the next level, the four types of SPRY/CA

contacts are mixed and matched in a limited number of higher-order arrangements, which we observed as two (perhaps three) distinct classes of TRIM dihexagon-containing asymmetric units. These dihexagon units, in turn, form distinct patches of TRIM5α/CA superlattices. The patches are small because supercrystalline order or complementarity between the two component lattices can be only sustained over short distances. Last, the patches are connected by grain boundaries made of adjacent pentagons and heptagons, analogous to paracrystalline carbon arrays.

Further studies are now required to elucidate the dynamics of TRIM5α assembly on retroviral capsid templates. We envision that the "minimal recognition unit" of TRIM5α constitutes a ditriskelion—a central TRIM5α dimer with two "arms" at each end—which forms the central scaffold of the dihexagon. A ditriskelion satisfies all three functional requirements of capsid recognition: direct binding of the SPRY domain to CA, dimerization of the coiled coil, and higher-order assembly (trimerization) of the B-box 2 domain [reviewed in (*3*)]. A ditriskelion can act both as a molecular ruler (by matching the spacings, in a degenerate manner, of the arrayed SPRY domain dimers and CA hexamers) and as a protractor (because binding of the flanking arms locks the central dimer in its bound position and defines the local lattice vector of the assembling TRIM lattice relative to the underlying capsid lattice). We further envision that as assembly progresses, joining and locking of each additional TRIM5α dimer within a ditriskelion effectively constitute repeated measurements of the capsid lattice. This allows the growing TRIM lattice to detect changes in capsid surface curvature and adjust accordingly. The ability of TRIM5 to form pentagons and other shapes is also likely to be an important mechanism to accommodate sharp capsid surface declinations containing CA pentamers.

Although TRIM5α restriction is associated with nonproductive, accelerated uncoating of retroviral cores (*2*, *38*, *39*), the capsid lattice is intact in our reconstructions. This indicates that, contrary to previous reports (*40*–*42*), the TRIM5α cage may not be intrinsically destabilizing to the capsid. In support of this interpretation, a variety of studies have detected stable TRIM5α/capsid complexes in the cytoplasm under conditions where the proteasome or self-ubiquitination of TRIM5α is inhibited (*43*–*45*). These observations also imply that the proteasome or some ubiquitin-dependent cellular machinery is required to accelerate uncoating. We also found that stable complexes are formed in vitro when TRIM5α assembles de novo around preformed capsid-like particles, provided that the recently described capsid stability factor—inositol hexakisphosphate (*46*, *47*)—is present (fig. S7). Under nonrestricted infection conditions, reverse transcription inside the core is thought to induce uncoating (*48*–*51*), likely by increasing pressure from within that eventually ruptures the capsid (*52*). The capsid-binding inhibitor PF74 stabilizes a ruptured capsid (*53*, *54*) and delays uncoating in vitro despite continued reverse transcription (*54*). We propose that TRIM5α may also stabilize the capsid lattice against rising pressure from inside the core. Recruitment of proteasomes [or autophagosomes (*55*)] would then destroy the entire assemblage and halt reverse transcription. Under conditions where ubiquitination is inhibited, reverse transcription can proceed to completion within the TRIM5α-bound capsid (*43*). Nevertheless, virus replication remains restricted, perhaps because the surrounding TRIM5α cage would interfere with other functions of the capsid, such as engagement of nuclear import and integration machinery. Thus, we propose that cage formation constitutes the restriction mechanism of TRIM5α.

MATERIALS AND METHODS

Sample preparation

TRIM5α and HIV-1 CA proteins were purified, and recombinant TRIM5α/CA complexes were prepared as described (*7*, *8*). For this study, we used TRIM5α from African green monkey because this variant is active against HIV-1 and efficiently assembles into hexagonal lattices in vitro (*7*). The recombinant TRIM5α protein contained an L81F mutation in the RING domain that allows in vitro coassembly with HIV-1 CA more efficiently than wild type and does not affect the ubiquitination activity of the RING domain or overall restriction activity of the protein.

Data acquisition and processing

A 20-μl aliquot of the coassembled sample was mixed with an equal volume of 10-nm BSA Gold Tracer (Electron Microscopy Sciences); 3.5 μl was applied on glow-discharged C-flat grids (Protochips) and then plunge-frozen into liquid ethane. Cryotomograms were acquired using an FEI Titan Krios electron microscope operating at 300 kV and equipped with a Falcon II camera. Tilt series were collected using the data collection software Tomography 3.0 (FEI) with an angular range of −60° to +60°, an angular increment of 1°, defocus values of 2.5 to 4 μm, and a nominal magnification of ×29,000, which corresponds to a pixel (px) size of 2.92 Å. One dataset was collected at a defocus value of 9 μm and used to generate initial reference-free maps for the TRIM5α trimer and dimer. Tilt series were aligned by using IMOD (*56*). Weighted back-projection was used to reconstruct tomograms, and the contrast transfer function was applied in IMOD. Subtomogram averaging was carried out using the Dynamo software package (*57*).

Reconstruction of the CA hexamer

Subvolumes were extracted from 2× binned data in 100 × 100 × 100 px uniformly distributed along the length of each tube, spaced by 17 px (fig. S2A). Initial Euler angles were assigned on the basis of the centroid position of each volume relative to the tube axis ["backbone" as defined in Dynamo (*57*)]. Initial averaging was performed via six-dimensional search (16 iterations), applying no symmetry. The resulting average map of the tube segment was then used to determine the positions of CA hexamers throughout the length of each tube. Subvolumes of 64 × 64 × 64 px centered on these positions were then reextracted from the 2× binned tomograms and assigned initial Euler angles in reference to the tube axis. An initial hexamer search template was generated by averaging the subvolumes using only azimuthal refinement, applying sixfold symmetry. Subtomogram averaging was then performed separately for each tube, applying twofold symmetry, a low-pass filter of 30 Å, and default masks in Dynamo. Upon convergence, lattice maps were generated as described (*58*) and visually examined. Particles that were clearly misaligned and/or had very low cross-correlation values were discarded. After another round of averaging and examination, 9684 subvolumes were extracted from unbinned tomograms (128 × 128 × 128 px) and split into even/odd subsets. The two subsets were treated independently from this point forward. For each subset, an initial template was generated by averaging all particles according to the Euler angles and positions determined from the previous refinement. Four iterations of refinement were performed, applying a soft-edged spherical mask of 35-px radius and progressively narrower angular and positional search ranges. The final map was calculated with a low-pass filter of 20 Å.

Reconstruction of the TRIM5α dimer and trimer

Initial maps of the trimer and dimer were generated by hand-picking ~60 particles from a single tomogram (defocus value of 9 μm), assigning initial Euler angles in reference to the tube backbone as defined above, and performing one round of azimuthal refinement with three- or twofold symmetry, as appropriate. These maps were used as initial search templates for the each of the seven tubes, as described below.

For each tube, the optimized tube backbone was defined in reference to the refined CA hexamer positions. This, in turn, was used to generate a tubular mesh with a 50-px radius; this mesh oversampled the TRIM lattice by at least 25× for the dimer and 35× for the trimer. Subvolumes of 64 × 64 × 64 px whose centers were uniformly distributed on this mesh were extracted from 2× binned tomograms. Initial polar angles were assigned in reference to the tube backbone, whereas azimuthal angles were randomized. One iteration of azimuthal and positional refinement was performed, using the far-from-focus trimer and dimer models as search templates, again applying three- or twofold symmetry as appropriate and a low-pass filter of 40 Å (fig. S3A). The averaged maps from these first rounds were then used as search template in all subsequent refinements. In the first three iterations, refined positions that were within 4 px of each other were averaged, reextracted from the tomograms, and reassigned Euler angles as above. On the fourth iteration, lattice maps were examined, and particles that migrated to unrealistic positions and/or had very low cross-correlation values were discarded. Subvolumes were then reextracted (128 × 128 × 128 px) from unbinned tomograms (3204 dimers and 2108 trimers from seven tubes) and split into even/odd subsets, which were treated independently from this point forward. Refinement iterations were performed until convergence (which required six iterations for the dimer and eight for the trimer), with progressively narrower angular and positional search ranges and a low-pass filter set at 30 Å. Soft-edged tubular and ellipsoidal masks were used for the dimer and trimer, respectively.

Reconstruction of the TRIM5α/CA complex

Guided by the combined TRIM and CA lattice maps, 550 subvolumes encompassing entire TRIM hexagons were extracted (64 × 64 × 64 px) from 4× binned tomograms and assigned polar Euler angles in reference to the underlying CA lattice [which was modeled as "surface" in Dynamo (*57*)]. Azimuthal angles were randomized. One iteration of azimuthal refinement was performed to generate an initial model (fig. S6A). Classification was performed by multireference alignment in Dynamo, using as reference two copies of the initial model with random noise added, a cylindrical alignment mask that covered both the TRIM and CA densities, and a cylindrical classification mask that covered only the CA densities. The classification separated the particles into two classes (Classes 1 and 2) according to the rotation of the TRIM hexagon relative to the long axis of the tube (fig. S6, A and B). A second classification run was performed on the Class 2 particles, which further separated the particles into two subclasses (Classes 2a and 2b) that differed in translation of the TRIM hexagon relative to the underlying CA lattice (fig. S6, A and C). Class 1 particles from above (335 particles) were recropped from 2× binned tomograms (128 × 128 × 128 px) and refined for two additional iterations with progressively narrower angular and positional search ranges.

Fourier shell correlations

Correlations between the even/odd maps of the CA hexamer (fig. S2C), TRIM dimer (fig. S3E, blue curve), and TRIM trimer (fig. S3E, magenta curve) were calculated inside soft-edged Gaussian masks using the dfsc subroutine in Dynamo (*57*), and map "resolutions" were determined at the 0.143 gold standard cutoff (17.5, 25.7, and 24.9 Å for the hexamer, dimer, and trimer, respectively).

Resolution estimation for the Class 1 TRIM5α/CA complex was performed as follows. The central hexamer was aligned with the CA hexamer reconstruction as reference with Chimera (*59*), and the correlation between the two maps was calculated with the dfsc subroutine in Dynamo (fig. S6D, green curve) (*57*). The obtained 0.143 cutoff value was 23.8 Å. We also aligned each of the six hexagon edges with the TRIM dimer reconstruction as reference, which gave an average value of 31.7 ± 1.8 Å at the 0.143 cutoff (fig. S4B, blue curves).

Structural analysis and visualization

Map examination, PDB model fitting, and figure rendering were all performed with Chimera (*59*).

Data deposition

Maps were deposited at the EMDB with accession numbers EMD-20562 (CA hexamer), EMD-20563 (TRIM5α dimer), EMD-20564 (TRIM5α trimer), and EMD-20565 (TRIM5α/CA complex). A representative tomogram was also deposited with accession number EMD-20574.

SUPPLEMENTARY MATERIALS

Supplementary material for this article is available at http://advances.sciencemag.org/cgi/content/full/5/11/eaaw3631/DC1

Fig. S1. Gallery of TRIM5α-coated HIV-1 CA tubes analyzed in this study.
Fig. S2. Subtomogram averaging of the HIV-1 CA hexamer.
Fig. S3. Subtomogram averaging of the TRIM5α dimer and trimer.
Fig. S4. Molecular fitting of the TRIM5α dimer and trimer.
Fig. S5. Identification of the RING domain.
Fig. S6. Subtomogram averaging of the TRIM5α/CA complex.
Fig. S7. De novo assembly of TRIM5α cages around capsid-like particles in the presence of inositol hexakisphosphate.

View/request a protocol for this paper from *Bio-protocol*.

REFERENCES AND NOTES

1. M. Stremlau, C. M. Owens, M. J. Perron, M. Kiessling, P. Autissier, J. Sodroski, The cytoplasmic body component TRIM5α restricts HIV-1 infection in Old World monkeys. *Nature* **427**, 848–853 (2004).
2. M. Stremlau, M. Perron, M. Lee, Y. Li, B. Song, H. Javanbakht, F. Diaz-Griffero, D. J. Anderson, W. I. Sundquist, J. Sodroski, Specific recognition and accelerated uncoating of retroviral capsids by the TRIM5α restriction factor. *Proc. Natl. Acad. Sci. U.S.A.* **103**, 5514–5519 (2006).
3. B. K. Ganser-Pornillos, O. Pornillos, Restriction of HIV-1 and other retroviruses by TRIM5. *Nat. Rev. Microbiol.* **17**, 546–556 (2019).
4. B. K. Ganser-Pornillos, V. Chandrasekaran, O. Pornillos, J. G. Sodroski, W. I. Sundquist, M. Yeager, Hexagonal assembly of a restricting TRIM5α protein. *Proc. Natl. Acad. Sci. U.S.A.* **108**, 534–539 (2011).
5. J. G. Sanchez, K. Okreglicka, V. Chandrasekaran, J. M. Welker, W. I. Sundquist, O. Pornillos, The tripartite motif coiled-coil is an elongated antiparallel hairpin dimer. *Proc. Natl. Acad. Sci. U.S.A.* **111**, 2494–2499 (2014).
6. D. C. Goldstone, P. A. Walker, L. J. Calder, P. J. Coombs, J. Kirkpatrick, N. J. Ball, L. Hilditch, M. W. Yap, P. B. Rosenthal, J. P. Stoye, I. A. Taylor, Structural studies of postentry restriction factors reveal antiparallel dimers that enable avid binding to the HIV-1 capsid lattice. *Proc. Natl. Acad. Sci. U.S.A.* **111**, 9609–9614 (2014).
7. Y.-L. Li, V. Chandrasekaran, S. D. Carter, C. L. Woodward, D. E. Christensen, K. A. Dryden, O. Pornillos, M. Yeager, B. K. Ganser-Pornillos, G. J. Jensen, W. I. Sundquist, Primate TRIM5 proteins form hexagonal nets on HIV-1 capsids. *eLife* **5**, e16269 (2016).
8. J. M. Wagner, M. D. Roganowicz, K. Skorupka, S. L. Alam, D. Christensen, G. Doss, Y. Wan, G. A. Frank, B. K. Ganser-Pornillos, W. I. Sundquist, O. Pornillos, Mechanism of B-box 2 domain-mediated higher-order assembly of the retroviral restriction factor TRIM5α. *eLife* **5**, e16309 (2016).

9. B. K. Ganser, S. Li, V. Y. Klishko, J. T. Finch, W. I. Sundquist, Assembly and analysis of conical models for the HIV-1 core. *Science* **283**, 80–83 (1999).
10. S. Mattei, B. Glass, W. J. Hagen, H.-G. Kräusslich, J. A. Briggs, The structure and flexibility of conical HIV-1 capsids determined within intact virions. *Science* **354**, 1434–1437 (2016).
11. S. Mattei, F. K. Schur, J. A. Briggs, Retrovirus maturation — an extraordinary structural transformation. *Curr. Opin. Virol.* **18**, 27–35 (2016).
12. B. K. Ganser-Pornillos, U. K. von Schwedler, K. M. Stray, C. Aiken, W. I. Sundquist, Assembly properties of the human immunodeficiency virus type 1 CA protein. *J. Virol.* **78**, 2545–2552 (2004).
13. S. Li, C. P. Hill, W. I. Sundquist, J. T. Finch, Image reconstructions of helical assemblies of the HIV-1 CA protein. *Nature* **407**, 409–413 (2000).
14. I. J. Byeon, X. Meng, J. Jung, G. Zhao, R. Yang, J. Ahn, J. Shi, J. Concel, C. Aiken, P. Zhang, A. M. Gronenborn, Structural convergence between Cryo-EM and NMR reveals intersubunit interactions critical for HIV-1 capsid function. *Cell* **139**, 780–790 (2009).
15. W. Wan, J. A. Briggs, Cryo-electron tomography and subtomogram averaging. *Methods Enzymol.* **579**, 329–367 (2016).
16. J. M. Wagner, D. E. Christensen, A. Bhattacharya, D. M. Dawidziak, M. D. Roganowicz, Y. Wan, R. A. Pumroy, B. Demeler, D. N. Ivanov, B. K. Ganser-Pornillos, W. I. Sundquist, O. Pornillos, General model for retroviral capsid pattern recognition by TRIM5 proteins. *J. Virol.* **92**, e01563-17 (2018).
17. M. D. Roganowicz, S. Komurlu, S. Mukherjee, J. Plewka, S. L. Alam, K. A. Skorupka, Y. Wan, D. Dawidowski, D. S. Cafiso, B. K. Ganser-Pornillos, E. M. Campbell, O. Pornillos, TRIM5α SPRY/coiled-coil interactions optimize avid retroviral capsid recognition. *PLOS Pathog.* **13**, e1006686 (2017).
18. N. Biris, Y. Yang, A. B. Taylor, A. Tomashevski, M. Guo, P. J. Hart, F. Diaz-Griffero, D. N. Ivanov, Structure of the rhesus monkey TRIM5α PRYSPRY domain, the HIV capsid recognition module. *Proc. Natl. Acad. Sci. U.S.A.* **109**, 13278–13283 (2012).
19. H. Yang, X. Ji, G. Zhao, J. Ning, Q. Zhao, C. Aiken, A. M. Gronenborn, P. Zhang, Y. Xiong, Structural insight into HIV-1 capsid recognition by rhesus TRIM5α. *Proc. Natl. Acad. Sci. U.S.A.* **109**, 18372–18377 (2012).
20. S. Sebastian, C. Grütter, C. Strambio de Castillia, T. Pertel, S. Olivari, M. G. Grütter, J. Luban, An invariant surface patch on the TRIM5α PRYSPRY domain is required for retroviral restriction but dispensable for capsid binding. *J. Virol.* **83**, 3365–3373 (2009).
21. S. L. Sawyer, L. I. Wu, M. Emerman, H. S. Malik, Positive selection of primate TRIM5α identifies a critical species-specific retroviral restriction domain. *Proc. Natl. Acad. Sci. U.S.A.* **102**, 2832–2837 (2005).
22. N. Biris, A. Tomashevski, A. Bhattacharya, F. Diaz-Griffero, D. N. Ivanov, Rhesus monkey TRIM5α SPRY domain recognizes multiple epitopes that span several capsid monomers on the surface of the HIV-1 mature viral core. *J. Mol. Biol.* **425**, 5032–5044 (2013).
23. D. B. Kovalskyy, D. N. Ivanov, Recognition of the HIV capsid by the TRIM5α restriction factor is mediated by a subset of pre-existing conformations of the TRIM5α SPRY domain. *Biochemistry* **53**, 1466–1476 (2014).
24. M. É. Nepveu-Traversy, A. Demogines, T. Fricke, M. B. Plourde, K. Riopel, M. Veillette, F. Diaz-Griffero, S. L. Sawyer, L. Berthoux, A putative SUMO interacting motif in the B30.2/SPRY domain of rhesus macaque TRIM5α important for NF-κB/AP-1 signaling and HIV-1 restriction. *Heliyon* **2**, e00056 (2016).
25. T. Hatziioannou, S. Cowan, U. K. von Schwedler, W. I. Sundquist, P. D. Bieniasz, Species-specific tropism determinants in the human immunodeficiency virus type 1 capsid. *J. Virol.* **78**, 6005–6012 (2004).
26. C. M. Owens, B. Song, M. J. Perron, P. C. Yang, M. Stremlau, J. Sodroski, Binding and susceptibility to postentry restriction factors in monkey cells are specified by distinct regions of the human immunodeficiency virus type 1 capsid. *J. Virol.* **78**, 5423–5437 (2004).
27. H. Song, E. E. Nakayama, M. Yokoyama, H. Sato, J. A. Levy, T. Shioda, A single amino acid of the human immunodeficiency virus type 2 capsid affects its replication in the presence of cynomolgus monkey and human TRIM5αs. *J. Virol.* **81**, 7280–7285 (2007).
28. G. B. Mortuza, M. P. Dodding, D. C. Goldstone, L. F. Haire, J. P. Stoye, I. A. Taylor, Structure of B-MLV capsid amino-terminal domain reveals key features of viral tropism, *gag* assembly and core formation. *J. Mol. Biol.* **376**, 1493–1508 (2008).
29. K. Kono, H. Song, M. Yokoyama, H. Sato, T. Shioda, E. E. Nakayama, Multiple sites in the N-terminal half of simian immunodeficiency virus capsid protein contribute to evasion from rhesus monkey TRIM5α-mediated restriction. *Retrovirology* **7**, 72 (2010).
30. A. Kuroishi, K. Bozek, T. Shioda, E. E. Nakayama, A single amino acid substitution of the human immunodeficiency virus type 1 capsid protein affects viral sensitivity to TRIM5α. *Retrovirology* **7**, 58 (2010).
31. S. Ohkura, D. C. Goldstone, M. W. Yap, K. Holden-Dye, I. A. Taylor, J. P. Stoye, Novel escape mutants suggest an extensive TRIM5α binding site spanning the entire outer surface of the murine leukemia virus capsid protein. *PLOS Pathog.* **7**, e1002011 (2011).
32. K. R. McCarthy, A. G. Schmidt, A. Kirmaier, A. L. Wyand, R. M. Newman, W. E. Johnson, Gain-of-sensitivity mutations in a Trim5-resistant primary isolate of pathogenic SIV identify two independent conserved determinants of Trim5α specificity. *PLOS Pathog.* **9**, e1003352 (2013).
33. S. Ohkura, J. P. Stoye, A comparison of murine leukemia viruses that escape from human and rhesus macaque TRIM5αs. *J. Virol.* **87**, 6455–6468 (2013).
34. C. Ophus, A. Shekhawat, H. Rasool, A. Zettl, Large-scale experimental and theoretical study of graphene grain boundary structures. *Phys. Rev. B* **92**, 205402 (2015).
35. C. Gong, K. He, Q. Chen, A. W. Robertson, J. H. Warner, *In situ* high temperature atomic level studies of large closed grain boundary loops in graphene. *ACS Nano* **10**, 9165–9173 (2016).
36. O. Pornillos, B. K. Ganser-Pornillos, M. Yeager, Atomic-level modelling of the HIV capsid. *Nature* **469**, 424–427 (2011).
37. P. I. Kitov, D. R. Bundle, On the nature of the multivalency effect: A thermodynamic model. *J. Am. Chem. Soc.* **125**, 16271–16284 (2003).
38. M. J. Perron, M. Stremlau, M. Lee, H. Javanbakht, B. Song, J. Sodroski, The human TRIM5α restriction factor mediates accelerated uncoating of the N-tropic murine leukemia virus capsid. *J. Virol.* **81**, 2138–2148 (2007).
39. S. B. Kutluay, D. Perez-Caballero, P. D. Bieniasz, Fates of retroviral core components during unrestricted and TRIM5-restricted infection. *PLOS Pathog.* **9**, e1003214 (2013).
40. C. R. Langelier, V. Sandrin, D. M. Eckert, D. E. Christensen, V. Chandrasekaran, S. L. Alam, C. Aiken, J. C. Olsen, A. K. Kar, J. G. Sodroski, W. I. Sundquist, Biochemical characterization of a recombinant TRIM5α protein that restricts human immunodeficiency virus type 1 replication. *J. Virol.* **82**, 11682–11694 (2008).
41. L. R. Black, C. Aiken, TRIM5α disrupts the structure of assembled HIV-1 capsid complexes in vitro. *J. Virol.* **84**, 6564–6569 (2010).
42. G. Zhao, D. Ke, T. Vu, J. Ahn, V. B. Shah, R. Yang, C. Aiken, L. M. Charlton, A. M. Gronenborn, P. Zhang, Rhesus TRIM5α disrupts the HIV-1 capsid at the inter-hexamer interfaces. *PLOS Pathog.* **7**, e1002009 (2011).
43. J. L. Anderson, E. M. Campbell, X. Wu, N. Vandegraaff, A. Engelman, T. J. Hope, Proteasome inhibition reveals that a functional preintegration complex intermediate can be generated during restriction by diverse TRIM5 proteins. *J. Virol.* **80**, 9754–9760 (2006).
44. E. M. Campbell, O. Perez, J. L. Anderson, T. J. Hope, Visualization of a proteasome-independent intermediate during restriction of HIV-1 by rhesus TRIM5α. *J. Cell Biol.* **180**, 549–561 (2008).
45. E. M. Campbell, J. Weingart, P. Sette, S. Opp, J. Sastri, S. K. O'Connor, S. Talley, F. Diaz-Griffero, V. Hirsch, F. Bouamr, TRIM5α-mediated ubiquitin chain conjugation is required for inhibition of HIV-1 reverse transcription and capsid destabilization. *J. Virol.* **90**, 1849–1857 (2015).
46. R. A. Dick, K. K. Zadrozny, C. Xu, F. K. M. Schur, T. D. Lyddon, C. L. Ricana, J. M. Wagner, J. R. Perilla, B. K. Ganser-Pornillos, M. C. Johnson, O. Pornillos, V. M. Vogt, Inositol phosphates are assembly co-factors for HIV-1. *Nature* **560**, 509–512 (2018).
47. D. L. Mallery, C. L. Márquez, W. A. McEwan, C. F. Dickson, D. A. Jacques, M. Anandapadamanaban, K. Bichel, G. J. Towers, A. Saiardi, T. Böcking, L. C. James, IP6 is an HIV pocket factor that prevents capsid collapse and promotes DNA synthesis. *eLife* **7**, e35335 (2018).
48. A. E. Hulme, O. Perez, T. J. Hope, Complementary assays reveal a relationship between HIV-1 uncoating and reverse transcription. *Proc. Natl. Acad. Sci. U.S.A.* **108**, 9975–9980 (2011).
49. Y. Yang, T. Fricke, F. Diaz-Griffero, Inhibition of reverse transcriptase activity increases stability of the HIV-1 core. *J. Virol.* **87**, 683–687 (2013).
50. O. Cosnefroy, P. J. Murray, K. N. Bishop, HIV-1 capsid uncoating initiates after the first strand transfer of reverse transcription. *Retrovirology* **13**, 58 (2016).
51. J. I. Mamede, G. C. Cianci, M. R. Anderson, T. J. Hope, Early cytoplasmic uncoating is associated with infectivity of HIV-1. *Proc. Natl. Acad. Sci. U.S.A.* **114**, E7169–E7178 (2017).
52. S. Rankovic, J. Varadarajan, R. Ramalho, C. Aiken, I. Rousso, Reverse transcription mechanically initiates HIV-1 capsid disassembly. *J. Virol.* **91**, e00289-17 (2017).
53. C. L. Márquez, D. Lau, J. Walsh, V. Shah, C. McGuinness, A. Wong, A. Aggarwal, M. W. Parker, D. A. Jacques, S. Turville, T. Böcking, Kinetics of HIV-1 capsid uncoating revealed by single-molecule analysis. *eLife* **7**, e34772 (2018).
54. S. Rankovic, R. Ramalho, C. Aiken, I. Rousso, PF74 reinforces the HIV-1 capsid to impair reverse transcription-induced uncoating. *J. Virol.* **92**, e00845-18 (2018).
55. M. A. Mandell, A. Jain, J. Arko-Mensah, S. Chauhan, T. Kimura, C. Dinkins, G. Silvestri, J. Münch, F. Kirchhoff, A. Simonsen, Y. Wei, B. Levine, T. Johansen, V. Deretic, TRIM proteins regulate autophagy and can target autophagic substrates by direct recognition. *Dev. Cell* **30**, 394–409 (2014).
56. J. R. Kremer, D. N. Mastronarde, J. R. McIntosh, Computer visualization of three-dimensional image data using IMOD. *J. Struct. Biol.* **116**, 71–76 (1996).
57. D. Castaño-Díez, M. Kudryashev, M. Arheit, H. Stahlberg, Dynamo: A flexible, user-friendly development tool for subtomogram averaging of cryo-EM data in high-performance computing environments. *J. Struct. Biol.* **178**, 139–151 (2012).
58. S. Mattei, A. Tan, B. Glass, B. Müller, H.-G. Kräusslich, J. A. G. Briggs, High-resolution structures of HIV-1 Gag cleavage mutants determine structural switch for virus maturation. *Proc. Natl. Acad. Sci. U.S.A.* **115**, E9401–E9410 (2018).
59. E. F. Pettersen, T. D. Goddard, C. C. Huang, G. S. Coouch, D. M. Greenblatt, E. C. Meng, T. E. Ferrin, UCSF Chimera—A visualization system for exploratory research and analysis. *J. Comput. Chem.* **25**, 1605–1612 (2004).

Acknowledgments: We thank D. Castaño-Diez, F. Schur, and J. Briggs for advice on subtomogram averaging; W. Sundquist, J. McCullough, and members of our laboratories for critical reading of the manuscript. We thank K. Dryden for expert technical assistance with cryo–electron microscopy data collection and helpful discussions. The cryo–electron microscopy imaging conducted at the Molecular Electron Microscopy Core facility at the University of Virginia was supported by the School of Medicine and built with NIH grant G20-RR31199. The Titan Krios and Falcon II direct electron detectors were obtained with NIH grants S10-RR025067 and S10-OD018149, respectively. **Funding:** This work was supported by NIH grants R01-GM112508/AI150479 (O.P.) and P50-GM082545/AI150464 (B.K.G.-P.). **Author contributions:** K.A.S., M.D.R., D.E.C., Y.W., O.P., and B.K.G.-P.: investigation, methodology, validation, and writing (review and editing); K.A.S., O.P., and B.K.G.-P.: formal analysis, visualization, and writing (original draft); O.P., and B.K.G.-P.: conceptualization, funding acquisition, and supervision. **Competing interests:** The authors declare that they have no competing interests. **Data and materials availability:** All data needed to evaluate the conclusions in the paper are present in the paper and/or the Supplementary Materials. Averaged maps and a representative tomogram are deposited in the EMDB under accession numbers EMD-20562, EMD-20563, EMD-20546, EMD-20565, and EMD-20574. Additional data related to this paper may be requested from the authors.

Submitted 12 December 2018
Accepted 7 October 2019
Published 27 November 2019
10.1126/sciadv.aaw3631

Citation: K. A. Skorupka, M. D. Roganowicz, D. E. Christensen, Y. Wan, O. Pornillos, B. K. Ganser-Pornillos, Hierarchical assembly governs TRIM5α recognition of HIV-1 and retroviral capsids. *Sci. Adv.* **5**, eaaw3631 (2019).